Chinese Chemical Letters 35 (2024) 109634

Contents lists available at ScienceDirect

Chinese Chemical Letters

journal homepage: www.elsevier.com/locate/cclet

Laser constructed vacancy-rich TiO_{2-x}/Ti microfiber *via* enhanced interfacial charge transfer for operando extraction-SERS sensing

Ying Hou[a,1], Zhen Liu[a,1,*], Xiaoyan Liu[a], Zhiwei Sun[a], Zenan Wang[c], Hong Liu[a,b,*], Weijia Zhou[a,*]

[a] Institute for Advanced Interdisciplinary Research (iAIR), School of Chemistry and Chemical Engineering, University of Jinan, Ji'nan 250022, China
[b] State Key Laboratory of Crystal Materials, Shandong University, Ji'nan 250100, China
[c] Shenzhen Institute of Advanced Technology, Chinese Academy of Sciences, Shenzhen 518055, China

ARTICLE INFO

Article history:
Received 19 December 2023
Revised 5 February 2024
Accepted 7 February 2024
Available online 9 February 2024

Keywords:
Defect engineering
TiO_{2-x}/Ti microfiber
Laser microfabrication
Surface-enhanced Raman scattering
Solid phase microextraction
Operando sensing

ABSTRACT

Semiconductor-molecule surface-enhanced Raman scattering (SERS), especially the stronger interfacial charge transfer process (ICTP), represents a frontier in the field of SERS with spectral reproducibility and unparalleled selectivity. Herein, through a laser microfabrication method *in situ*, the free-standing, super hydrophilic and vacancy-rich TiO_{2-x}/Ti is successfully synthesized. Using blue TiO_x/Ti (B-TiO_x/Ti) as pre-concentrated substrate, a nanomolar-level limit of detection of 12 nmol/L at 1385 cm^{-1}, is confirmed using crystal violet (CV) bacteriostat as a model under 532 nm excitation. Furthermore, the results demonstrate that the SERS enhancement mechanism is *via* the moderate adulteration of oxygen vacancy, which leads to a narrow value of band gap and increases the ICTP of substrate to molecules. Using a hand-held extractor assembled with B-TiO_x/Ti microfiber, the operando analysis of mixtures distributed information excited in different parts of Asian carp is facilely achieved. This work guides the controlled synthesis of vacancy-rich TiO_{2-x}/Ti nanostructure and its application in ultrasensitive extraction-SERS detection. It also provides the direction for the rapid and operando transmission of biological information with temporal and spatial concentration distribution in human tissues by highly sensitized materials.

Surface-enhanced Raman scattering (SERS), a powerful analytical methodology, is deemed to "molecular fingerprint" characteristic and "label-free" trace recognition with advantages of sensitive, reliable, non-destructive, rapid and quantitative detection [1–3]. SERS has been extensively applied in multiple fields such as surface/interface science [4], bio-detection [5], medical diagnosis [6], environmental monitoring [7] and chemical analysis [8]. SERS enhancement mechanism can be generally attributed to a combination of electromagnetic mechanism (EM) of nanostructured localized surface plasmon resonance (LSPR) by noble metals [9] and chemical mechanism (CM) of chemical bonding interaction between the adsorbate and substrate [10,11]. Especially, semiconductor materials of CM explanation have aroused wide-spread concern with the advantages of more flexible controllability and enhanced selectivity of target molecules, such as TiO_2 [12], Ta_2O_5 nanorods [13], VO_2 nanosheets [14], ZnO nanorods [15] and urchin-like WO_3 [11,16]. The interfacial charge transfer process (ICTP) resonance can be enhanced by regulating the exciton Bohr radius, band structure, element doping, electron density, surface chemical stability, stoichiometry, geometry and crystallinity [17–19]. However, the limit of detection (LOD) and Raman enhancement factor (EF) of metal oxides semiconductor substrates are still to be improved compared to those of noble-metal structures. Therefore, the exploration of optimized substrate to improve the ICTP efficiency is particularly important [20,21].

TiO_2 semiconductor nanomaterial has attracted increasing interest with the advantages of chemical stability, nontoxicity and low price [22–25], but was suffered from ultraviolet light spectral range due to the wide band gap at −3.0 eV and −3.2 eV corresponding to rutile and anatase, which prejudiced the charge transfer (CT) from TiO_2 to the probe molecule and caused the limitation of the SERS effect [26]. Thus, TiO_2 was designed by band structure, and surface physicochemical properties to elevate the ICTP efficiency, which led to an improved SERS activity. Recently, oxygen vacancy-rich defect engineering and element doping have been proved to remarkably promote electron transportation and provides more active sites [27–30]. For instance, Guo *et al* [12]. synthesized amor-

* Corresponding authors.
E-mail addresses: mse_liuz@ujn.edu.cn (Z. Liu), hongliu@sdu.edu.cn (H. Liu), ifc_zhouwj@ujn.edu.cn (W. Zhou).
[1] These authors contributed equally to this work.

https://doi.org/10.1016/j.cclet.2024.109634
1001-8417/

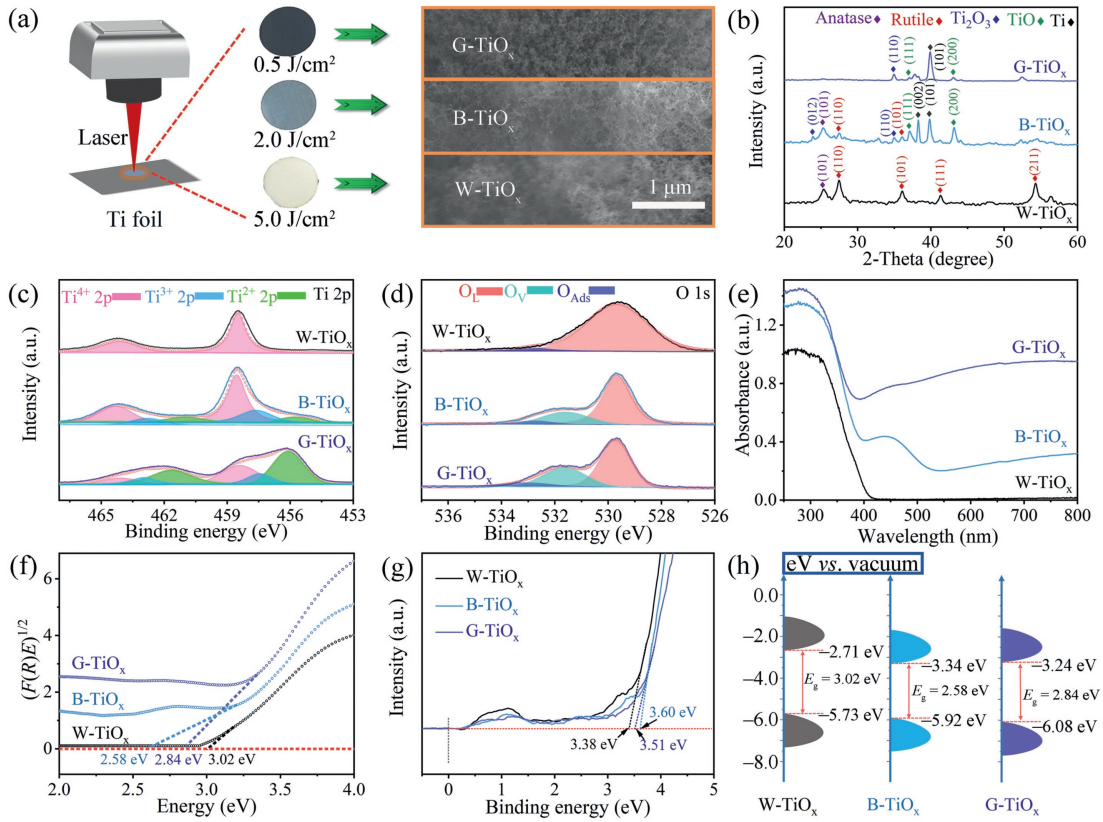

Fig. 1. (a) Schematic diagram of TiO_{2-x}/Ti nanostructures synthesized by laser and corresponding FESEM images. (b) XRD patterns of TiO_{2-x}/Ti prepared with different laser fluences. (c) Ti 2p and (d) O 1s spectra of W-TiO_x, B-TiO_x and G-TiO_x in XPS analysis. (e) UV–vis curves, the corresponding plots of $(F(R)E)^{1/2}$ (f), UPS spectra (g) and the proposed band structure (h) for W-TiO_x, B-TiO_x, and G-TiO_x.

phous TiO_2 nanosheet as SERS substrate, which had an high EF of 1.86×10^6 with optimized band structure and better electronic density of states (DOS). Unsaturated coordination of surface titanium (Ti) atoms and abundant surface oxygen allowed significant CT from the combined molecule to semiconductor TiO_2 nanosheet. These discoveries promised us to make the best of ICTP to enhance the SERS sensitivity through controlling the defect sites of TiO_2.

Because of the ultra-concentrated energy density and high local thermal effect, laser microfabrication gradually emerged as an efficient construction way through the laser heating directly on the different metal surfaces, which was constructed with the advantages of controlled laser patterning design, mass preparation, synthetic stacking faults suprananoparticles and providing abundant reaction sites [31–34]. In light of the above considerations, herein, we exhibited a preparative method *in situ via* laser for rapid synthesis of oxygen vacancy-rich TiO_{2-x}/Ti nanostructure. The synthesized TiO_{2-x}/Ti was used as the extraction-SERS substrate for the preconcentration and detection of the bacteriostat crystal violet (CV) and the EF reached to 1.82×10^6. The SERS enhancement mechanism was confirmed by experiments and DFT calculations. Unsaturated coordination of surface Ti atoms and oxygen vacancy generated by the high pulsed laser energy and local thermal effect, led to a narrow value of the band gap and high carrier mobility. The satisfied results obtained in mixture samples showed that the vacancy-rich B-TiO_x/Ti substrate had practical value in extraction-SERS application. This work provides valuable guidelines for preparing and exploring defect engineering of other typical 2D transition metal oxide, such as Ta_2O_5, VO_2 and ZnO nanorods.

The synthesis of vacancy TiO_{2-x}/Ti nanostructures was performed by laser on Ti foil at ambient atmosphere. As shown in Fig. 1a, the representative colors of TiO_{2-x} coatings were grey blue, blue and white at laser of 0.5 J/cm^2, 2.0 J/cm^2 and 5.0 J/cm^2 with little size difference in field emission scanning electron microscope (FESEM) images, which was ablated with laser fluences of heating effect (Fig. S1 in Supporting information, according temperature about 280 °C, 350 °C and 850 °C), named as G-TiO_x, B-TiO_x, W-TiO_x, respectively. The morphology of the prepared TiO_{2-x} nanostructures were sea urchin-like aggregates (Fig. S2 in Supporting information). Transmission electron microscope (TEM) images of TiO_{2-x} showed that the legible nanoparticles were spherical morphology and diameter was 10–50 nm (Figs. S3a–c in Supporting information). The X-ray diffraction (XRD) patterns of TiO_{2-x}/Ti nanostructure in Fig. 1b showed that the B-TiO_x was composed of rutile phase (PDF#72–1148) with characteristic peaks at 27.4° (110), 36.0° (101), anatase phase (PDF#71–1167) with characteristic peak at 25.3° (101), Ti_2O_3 phase (PDF#71–1057) with characteristic peaks at 23.9° (012), 34.9° (110), and TiO phase (PDF#77–2170) with the characteristic peaks at 37.1° (111) and 43.2° (200). In addition, the Ti substrate (PDF#44–1294) was also detected at 38.3° (002) and 40.1° (101). When the laser fluences decreased, the crystal patterns transferred to the mixed phase (G-TiO_x), which was composed of Ti_2O_3 and TiO. When the laser fluences increased, the crystal patterns of W-TiO_x became to be mixed phases of rutile and anatase. The images of high-resolution TEM (HRTEM) exhibited a mixed crystalline structure clearly (Figs. S3d–f in Supporting information). The obvious lattice fringes of 0.35 nm and 0.32 nm were recognized as (101) plane and (110) plane of anatase and rutile TiO_2. The (200) plane of TiO lattice fringe was identified of 0.20 nm. For B-TiO_x, the TiO phase grown along the crystal grain of TiO_2 (Fig. S3e in Supporting information). High-angle annular dark-

field scanning TEM (HAADF-STEM) image was further employed to confirm the composition of TiO_{2-x} (Fig. S3g in Supporting information). The elemental mapping was demonstrated that the nanostructure was comprised of Ti (Fig. S3h in Supporting information) and O (Fig. S3i in Supporting information) onto the surface and margin of the nanostructure. The Raman spectra simultaneously used to verify the composition and structure of TiO_{2-x} nanostructures (Fig. S4 in Supporting information).

X-ray photoelectron spectroscopy (XPS) results verified that the clearly Ti and O characteristic peaks existed in both of the W-TiO_x, B-TiO_x and G-TiO_x (Fig. S5 in Supporting information). The two spin-orbit splits of Ti $2p_{1/2}$ and Ti $2p_{3/2}$ at 464.1 and 458.4 eV were assigned to Ti^{4+} spices for W-TiO_x (Fig. 1c) [35]. Two other pairs of corresponding peaks could be observed at the B-TiO_x and G-TiO_x. The characteristic peaks at 462.7 and 457.5 eV were assigned to the Ti 2p of Ti^{3+} spices in B-TiO_x, and the characteristic peaks at 461.1 and 455.7 eV were classified into the Ti 2p of Ti^{2+} spices [36]. However, the Ti 2p (Ti^{2+}) peak of G-TiO_x shifted to the high position at nearly 0.4 eV, which was most likely due to the relatively less pulsed laser energy and local thermal effect compared with W-TiO_x and B-TiO_x. The O 1s spectra revealed that all the samples have the lattice oxygen of TiO_2 and absorbed hydroxyl oxygen at 529.7 eV and 532.8 eV (Fig. 1d). The characteristic peak at 531.7 eV was consistent with oxygen species adsorbed in vacancies of B-TiO_x and G-TiO_x [34], which was consistent with the result of Ti 2p, indicating the increasing oxygen vacancy concentration under non-equilibrium condition with change of laser irradiation. Electron paramagnetic resonance (EPR) was used to confirm the existence of more oxygen vacancy in TiO_{2-x}. B-TiO_x and G-TiO_x owned a stronger EPR signal at around $g = 2.005$ compared with W-TiO_x (Fig. S6 in Supporting information), indicating that rich oxygen vacancies were introduced into B-TiO_x and G-TiO_x [37,38].

The absorption spectra of laser-annealed defect TiO_{2-x} were shown in Fig. 1e. The W-TiO_x only showed UV region absorption at wavelengths below 380 nm, while the B-TiO_x and G-TiO_x exhibited absorption spectra that were red-shifted to the full visible light spectra. In addition, the light absorption after the wavelength at 420 nm increased as the reduction of laser energy, which was consistent with the formation of Ti^{2+} and Ti^{3+} in the defect TiO_2 basal surface [39]. To determine the band gap of the samples, Kubelka–Munk function method [40] was used to plot UV–vis diffuse reflectance spectra (Fig. 1f), *i.e.*, the spectra of converted $(F(R)E)^{1/2}$ *versus* E, in which $F(R) = (1-R)^2/2R$ and $E = h\nu$. R, h and ν are the reflectance, Planck constant and photon frequency, respectively. By measuring the inter sections of the extrapolated the linear regime and the photon energy E, the band gap values (E_g) were 2.84, 2.58 and 3.02 eV for G-TiO_x, B-TiO_x and W-TiO_x, respectively. It was probably owing to involvement of unsaturated coordination of surface Ti atoms and oxygen vacancy induced on the surface of TiO_2 [41] with suitable pulse energy, which resulted an enhanced absorption of photon energy and a narrow value of band gap [42]. Furthermore, the conduction band energy (E_C) and valence band energy (E_V) of TiO_2 were impacted by the O 2p and Ti 3d orbits. Ultraviolet photo-electron spectroscopy (UPS) was used to identify the ionization potential of G-TiO_x, B-TiO_x and W-TiO_x and the valance band maximum (E_{VBM}) was calculated to be 6.08, 5.92, and 5.73 eV by subtracting the width of the He I UPS spectra (Fig. 1g and Fig. S7 in Supporting information) from the excitation energy (21.22 eV). Thus, the conduction band minimum (E_{CBM}) of G-TiO_x, B-TiO_x and W-TiO_x were estimated at 3.24, 3.34 and 2.71 eV from $E_{VBM} - E_g$. Furthermore, characteristic peak was exhibited in the range of 0–2 eV (Fig. 1g), which was assigned to surface defects of oxygen vacancies from the lower oxidation state of Ti atom [43]. The result was consistent with the XPS analysis. Compared with W-TiO_x, E_V and E_C of defect B-TiO_x were continuum and overlapping, and a more negative E_{CBM} was possessed (Fig. 1h) [44]. The surface defects of the TiO_{2-x} would provide active sites on the surface, where would occur the reactant's special adsorption and reduce the barrier in the CT.

The SERS response of CV was investigated by incubating in 1 μmol/L working solution for 10 min at 25 °C (Fig. 2a). Compared with W-TiO_x and G-TiO_x, the Raman band had the most significant response on B-TiO_x from 400 cm^{-1} to 1600 cm^{-1}. The characteristic peaks appeared at 334 cm^{-1}, 418 cm^{-1}, 438 cm^{-1} 525 cm^{-1}, 563 cm^{-1}, 723 cm^{-1}, 757 cm^{-1}, 798 cm^{-1}, 911 cm^{-1}, 1175 cm^{-1}, 1296 cm^{-1}, 1366 cm^{-1}, 1537 cm^{-1}, 1586 cm^{-1} and 1617 cm^{-1}, agreed well with the Raman spectrum of solid powders of CV (Fig. S8 in Supporting information). The according enhancement factor of B-TiO_x was calculated to be 1.82×10^6 at 1385 cm^{-1} (Fig. 2b). In addition, the TiO_{2-x} substrates have also been used for the extraction and detection of auramine O (AO), chrysoidin (CS) and malachite green (MG), respectively (Figs. S9a–c in Supporting information). The detailed assignment of the vibrational band was shown in Table S1 (Supporting information). The characteristic SERS band at 939 cm^{-1} (AO), 1170 cm^{-1} (CS), 1392 cm^{-1} (MG) and 1385 cm^{-1} (CV) were caused by the $\delta(CC_{center}C)/\nu(CC_{center}C)/\nu(CN)$, $\delta(CCC)/\delta(CH)_{ring}$, $\delta(CH)/\delta(CH_3)/\delta(CCC)_{ring}$ and $\delta(CH)/\delta(CH_3)/\delta(CCC)_{ring}$, respectively [45–48]. These results indicated that molecules could be detected sensitively on the surface of B-TiO_x using SERS spectra. The enhancement factors were calculated as 4.85×10^6, 4.92×10^6 and 5.89×10^6 for AO, CS and MG respectively (Fig. S9d in Supporting information).

The stability of the prepared B-TiO_x substrate probed with CV was examined, which was a vital property of SERS-active substrate to assure convictive signal of quantitative detection. SERS band of CV were continuously recorded for 6 min (the integration time 1 s) with a laser power of 500 mW. As displayed in Fig. 2c, a stationary state of SERS intensity was maintained under continuous irradiation for 6 min. The relative standard deviation (RSD) of characteristic SERS spectrum intensities was 3.98% at 1175 cm^{-1}. Similarly, there was no obvious change in SERS intensity for AO, CS and MG, and the values of RSD were calculated as 3.98% at 939 cm^{-1}, 3.63% at 1147 cm^{-1} and 3.63% at 1392 cm^{-1}, respectively (Fig. S10 in Supporting information). This meant that the prepared B-TiO_x could be used for SERS analysis.

The terminal amino groups of four bacteriostats were protonated in aqueous solution to take the positive charge on nitrogen atom, which was easily adsorbed on TiO_{2-x}. Aniline derivatives featuring positive charged species can serve as antipode on the electric double layer interface for nanoparticle-molecule interaction. The pH response ranged from 2.0 to 10.0 in the extraction solution has been investigated. The incubated solution formed insoluble aggregates with the pH increased from 2.0 to 5.0, and the SERS spectrum of CS remained relatively stable in this process (Fig. S11b in Supporting information). But when pH value exceeded 6.0, the band intensity of SERS decreased rapidly in the region from 6.0 to 10.0. Similarly, the threshold pH value of extraction for AO (Fig. S11a in Supporting information) and MG (Fig. S11c in Supporting information) were observed at 6.0, respectively. The spectral evolution showed that the intensity and width of the characteristic peaks increased significantly, which indicated that the Raman spectrum change was not caused by the structural occurred at the pH value exceed 5.0 (Fig. 2d). As the increased pH value from 5.0 to 10.0, the SERS response reduced to the minimum. These can be ascribed to the deprotonation of amino below their pK_a in an aqueous solution which would influence the affinity of the amino species to the negative charged surface (the pK_a of CS: 10.1, AO: 10.7, Mg: 6.9, CV: 5.93, respectively). The experimental test results indicated that the extraction was well regulated by both the elec-

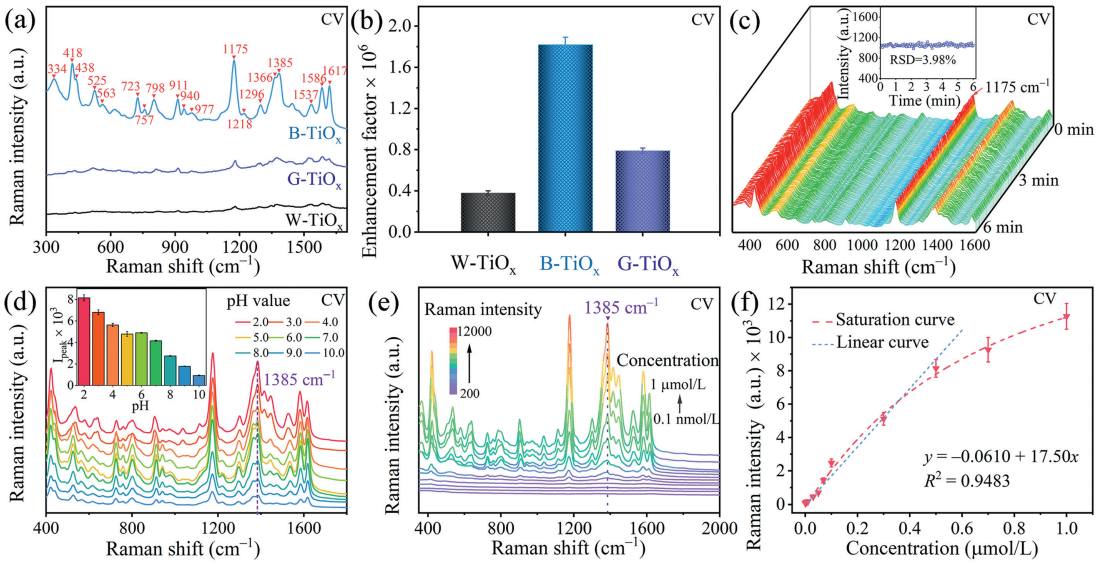

Fig. 2. (a) Raman spectra of CV at W-TiO$_x$, B-TiO$_x$ and G-TiO$_x$. (b) The corresponding histogram of enhancement factors. (c) Stability of the B-TiO$_x$ substrate with CV molecule for 6 min continuous laser radiations (Inset: The RSD at 1175 cm^{-1} with time). (d) pH response on the extraction (Inset: The Raman intensity at 1385 cm^{-1} with pH). (e) SERS spectra of characteristic peak *vs.* different concentration of CV (1 μmol/L–0.1 nmol/L). (f) The corresponding adsorption curves and the calibration curves.

trostatic and π-π interaction through the acidity of the solution at equilibrium.

The kinetic curves for AO, CS, CV, and MG with different concentrations (1.0, 0.1 and 0.01 μmol/L) were tested to evaluate the effect of extraction time. As exhibited in Fig. S12 (Supporting information), the time of saturated adsorption was between 10 min and 30 min for the four bacteriostats whatever the high and low concentration. Thus, the extraction time was extended to 60 min to remain the adsorption equilibrium of B-TiO$_x$ substrate and bacteriostats. According to the optimized test conditions, SERS spectra, corresponding adsorption curves and calibration curves were determined with saturated adsorption immersed into different concentrations (1 μmol/L–0.1 nmol/L) of CV (Figs. 2e and f), AO, CS and MG (Fig. S13 in Supporting information) with B-TiO$_x$, respectively. Raman intensity increased linearly at the concentration rang from 0.1 μmol/L to 0.1 nmol/L of CV at 1385 cm^{-1}, AO at 939 cm^{-1}, CS at 1170 cm^{-1} and MG at 1392 cm^{-1}. The correlation coefficient (R^2) was 0.9483, 0.9921, 0.9914 and 0.9673, and the LOD was 12 nmol/L, 9.8 nmol/L, 17 nmol/L and 14 nmol/L for CV, AO, CS and MG, respectively. In addition, the Raman intensity reached maximum with the increasing concentration, which could be attributed to the saturation adsorption of four bacteriostats on adsorption sites [49].

To investigate the SERS enhancement of the CM (including adsorbed CV molecular vibration and CT resonance) on this B-TiO$_x$ substrate, the resonance of CV@B-TiO$_x$ complex was decided through the UV–vis absorption spectra. Fig. 3a showed the adsorbed molecule CV existed a strong optical absorption peak at 532 nm near the laser excitation, which indicated an intrinsic molecular vibration (λ_{mol}) matching with the incident laser (λ_{laser}) at 532 nm. After forming CV@B-TiO$_x$ complex, the absorption peaks presented certain degrees of blueshift and broadening for CV@B-TiO$_x$ located in the wavelength range of 500–600 nm, indicating a strong chemical interaction and CT process between CV and B-TiO$_x$ substrate [50]. Thus, the quasi-resonant $\lambda_{CT} \approx \lambda_{laser}$ was valid in SERS, indicating the dominance of the CV process in the SERS [51].

The CV molecules can chemically adsorb onto the surface of B-TiO$_x$ *via* two potential sites, the positively charged nitrogen atoms of the imine can bond with the metal oxide crystal plane through the N-Ti and N-O bond. The model for rutile (110), anatase (101), Ti_2O_3 (110) and TiO (200) for B-TiO$_x$ were built and used to calculate the ICTP (Fig. S14 in Supporting information). PDOS calculation, differential charge density distribution (Fig. S15 in Supporting information) and the chemisorption energy ΔE_{chem} calculation (Table S2 in Supporting information) of CV@B-TiO$_x$ demonstrated a higher value of CV-Ti-TiO (200), indicating the most potential adsorption site on the surface was CV-Ti-TiO.

To investigate the electron transfer capability of molecules on the B-TiO$_x$ surface, the substantially enhanced energy level coupling in CV and various crystal planes of B-TiO$_x$ and greatly improved ICTP resonance within the surface of CV@B-TiO$_x$ complex were proved by DFT calculations. The HOMO–LUMO (Table S3 in Supporting information) of CV-Ti-crystal plane and CV-O-crystal plane bonds were also calculated, respectively. As was illustrated in Fig. 3b, HOMO and LUMO of CV filled the entire molecular structure. The surface CT complex CV@B-TiO$_x$ was formed by adsorption of CV molecule on various crystal planes rutile (110), anatase (101), Ti_2O_3 (110) and TiO (200) for B-TiO$_x$ surface. The results indicated that the LUMO of CV@Rutile (110), CV@Anatase (101), CV@Ti_2O_3 (110) complex were not bind on the entire CV@B-TiO$_x$ complex. In contrast, the charges for LUMO of the CV@TiO (200) complex were rearranged at the interface between CV and TiO, revealing excellent electron transfer ability from CV to the TiO (200). This clearly certified that the crystal plane TiO (200) of B-TiO$_x$ had a great regulation on the adsorbed CV molecular orbitals after forming the surface CT complex. Furthermore, the band gap of the CV molecule absorbed on CV@TiO (200) was 0.95 eV, which was clearly smaller than the HOMO–LUMO energy gap for CV (2.39 eV). This could be attributed to the strong energy level coupling between the CV molecule and the TiO crystal plane of B-TiO$_x$. According to the DFT calculation, it was showed that the surface CT complex of TiO exhibited more resonant excited states and higher PDOS *via* CV-Ti-TiO (Fig. 3c) and CV-N-Ti-TiO bonds (Fig. 3d), suggesting a high-efficient and potential CT process at the low-energy level, followed by enhanced Raman signals *via* N-Ti bonds. We further verified the above conclusions by differential charge density distribution (Figs. 3e–g). The distribution of electron accumulation (depletion) of N-Ti site for CV@TiO (200) illustrated a potential electron transfer channel with N-Ti (Fig. 3g).

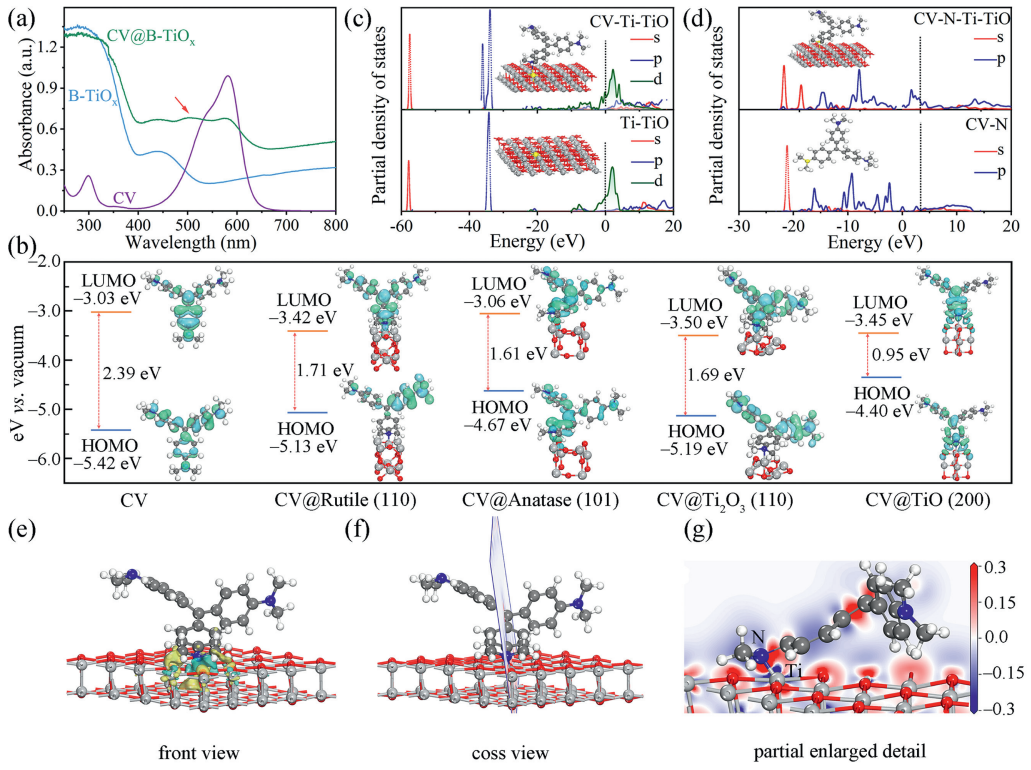

Fig. 3. (a) UV–vis absorption spectra of CV, B-TiO$_x$, and CV@B-TiO$_x$. (b) Energy level diagram of the HOMO and LUMO of CV, CV@Rutile (110), CV@Anatase (101), CV@Ti_2O_3 (110) and CV@TiO (200) for CV@B-TiO$_x$. PDOS calculation for TiO (200) surfaces absorbed by CV, including Ti-TiO and CV-Ti-TiO (c), and CV-N and CV-N-Ti-TiO (d). Differential charge density distribution of front view (e), coss view (f) and partial enlarged detail (g) for CV-Ti-TiO site of CV@B-TiO$_x$, the red (blue) distribution illustrates electron accumulation (depletion) of N-Ti site.

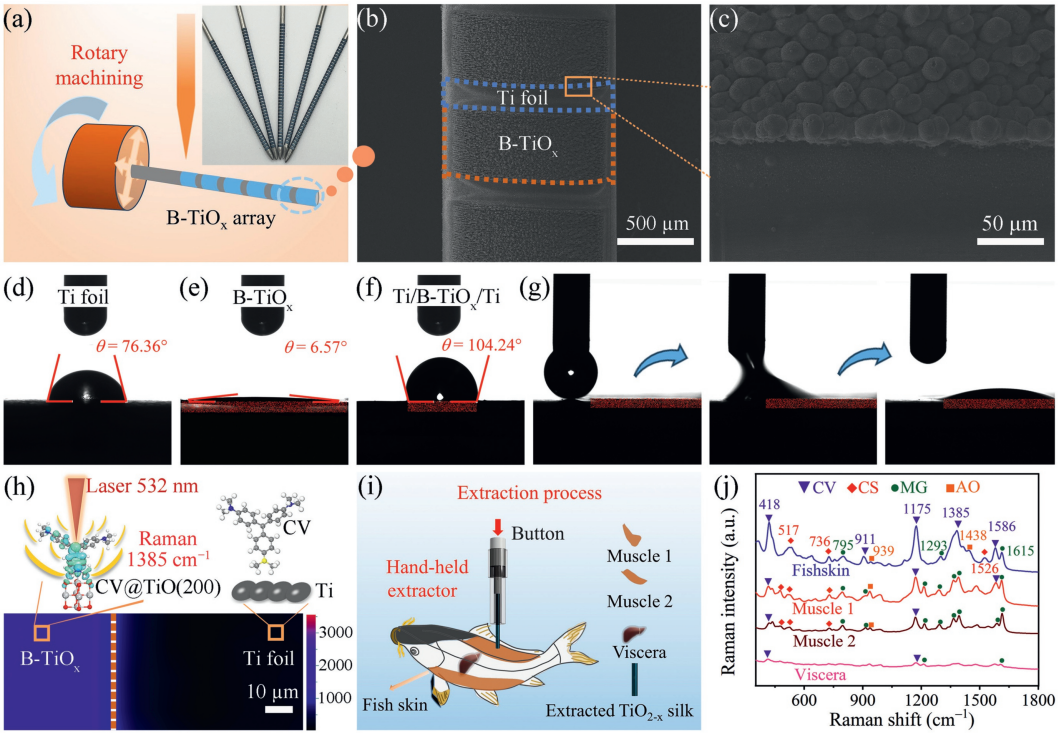

Fig. 4. (a) Schematic diagram of the B-TiO$_x$/Ti preparation process (Inset: real extracted B-TiO$_x$/Ti). (b) SEM image of extracted B-TiO$_x$/Ti microfiber and (c) partial enlarged detail of B-TiO$_x$ and Ti interface. The surface contact angle tests of the (d) Ti, (e) B-TiO$_x$ and (f) Ti/B-TiO$_x$/Ti with the size of 1.0 mm^2 for local B-TiO$_x$ nanostructure. (g) The contact angle of droplet dynamic process at the interface between Ti and B-TiO$_x$. (h) Raman image of B-TiO$_x$/Ti. (i) Schematic diagram of the extraction process by a hand-held extractor into polluted fish. (j) SERS spectra of the mixture containing distribution in the epidermis, muscle and viscera.

The one-step laser irradiation technology was used to prepare B-TiO_x on the Ti silk (diameter: 1.0 mm) (Fig. 4a). Fig. 4b was SEM image of B-TiO_x/Ti microfiber, which showed the periodic array structure. Fig. 4c displayed partial enlarged detail of B-TiO_x and Ti interface. For SERS detection of ultra-low concentration samples, higher requirements were put forward for the sensing substrates and detection methods. A battery of surface contact angle measurements was performed to verify the hydrophilicity of TiO_{2-x} and Ti substrates. It was 6.57° for B-TiO_x, indicating the super hydrophilic property, while the contact angle of Ti was 76.36° indicating the relatively hydrophobic surface (Figs. 4d and e). It was significant that in a local sample of B-TiO_x nanostructure (named Ti/B-TiO_x/Ti) with the size of 1.0 mm^2 on Ti substrate, the water accumulated completely at the location of B-TiO_x nanostructure and did not overflow the boundary between the B-TiO_x and Ti. This was attributed to the hydrophilicity of B-TiO_x and relative hydrophobicity of Ti substrate (Fig. 4f). Subsequently, the dynamic solid-drop contact angle test at the junction of B-TiO_x and Ti was also shown in Fig. 4g. The droplet's spontaneous tilt and strong movement toward the B-TiO_x region also demonstrated the more hydrophilic than that of Ti surface, which was beneficial to achieve the preconcentration of the measured substances in the extraction process and improved the sensitivity effectively. The SERS capability of the B-TiO_x/Ti was verified *via* Raman image in Fig. 4h.

To measure the capacity of detecting mixtures with defect B-TiO_x, the mixed sample was dissolved in 10 L (mixed thoroughly with 10 mL free range solution of each CV, AO, CS and MG). After a 100 g weight Asian carp was farmed in this polluted water for a week, the extraction process was performed for 60 min with a hand-held extractor (schematic diagram, Fig. 4i). SERS spectra of fish skin, two parts of muscle and viscera was shown in Fig. 4j. The bands at 418 cm^{-1}, 911 cm^{-1}, 1175 cm^{-1}, 1385 cm^{-1}, 1586 cm^{-1} (purple triangles) were assigned to CV. The bands at 939 cm^{-1} and 1438 cm^{-1} (orange squares) were assigned to the characteristic bands of AO. The peaks of 476 cm^{-1}, 517 cm^{-1}, 736 cm^{-1} and 1526 cm^{-1} (red diamonds) were identified for CS. The SERS peaks of MG were identified at 795 cm^{-1}, 914 cm^{-1}, 1216 cm^{-1}, 1293 cm^{-1}, 1365 cm^{-1}, 1392 cm^{-1}, 1588 cm^{-1}, 1615 cm^{-1} (green dots). Compared with skin and muscle, only trace amounts of CV and MG can be detected in viscera. These results proved that the mixtures can be extracted and accurately identified on this hand-held extractor simultaneously, which clearly indicated the distribution of bacteriostats in fish and demonstrated a relatively high concentration in fish skin compared with muscle and viscera.

In summary, vacancy-rich TiO_{2-x} microfibers were successfully prepared *in situ via* the relatively high pulsed laser energy and local thermal effect. The results of experiment and DFT calculations confirmed that unsaturated coordination of surface Ti atoms and oxygen vacancy effect were dominantly responsible for the significant SERS response on TiO_{2-x} substrate for detection of CV. Substantial CT occurred between the strong analytes and TiO_{2-x}, which resulted an enhanced absorption of photon energy and a narrow value of band gap *via* the molecular transition and the vibronic coupling. Thus, the LOD of CV, AO, CS and MG extracted on B-TiO_x/Ti was achieved to 12 nmol/L, 9.8 nmol/L, 17 nmol/L and 14 nmol/L under the pre-concentration and optimal conditions, and the enhancement factors were 1.82×10^6, 4.85×10^6, 4.92×10^6 and 5.89×10^6, respectively. Finally, the efficient B-TiO_x/Ti extractor was used to extract bacteriostats from fish fed in contaminated water, which promoted detection capability and demonstrated the distribution of bacteriostats in different parts of the body. This work also has significant guiding implication to deliver biological information on concentration distribution in human tissues through highly sensitized materials.

Declaration of competing interest

The authors declare that they have no known competing financial interests or personal relationships that could have appeared to influence the work reported in this paper.

Acknowledgments

This work was supported by National Key Research and Development Program of China (No. 2023YFB3210400), Major Scientific and Technological Innovation Project of Shandong Province (No. 2021CXGC010603), Natural Science Foundation of Shandong Province (Nos. ZR2020QE057, ZR2020QE071, ZR2020LLZ006), and Innovative Team Project of Jinan (No. 2021GXRC019).

Supplementary materials

Supplementary material associated with this article can be found, in the online version, at doi:10.1016/j.cclet.2024.109634.

References

[1] Y. Lu, X. Zhang, L. Zhao, et al., Nat. Commun. 14 (2023) 5860.
[2] A. Garg, E. Mejia, W. Nam, P. Vikesland, W. Zhou, Small 18 (2022) 2204517.
[3] Z. He, T. Rong, Y. Li, et al., ACS Nano 16 (2022) 4072–4083.
[4] X. Wang, S. Huang, T. Huang, et al., Chem. Soc. Rev. 46 (2017) 4020–4041.
[5] C. Qiu, W. Zhang, Y. Zhou, et al., Chem. Eng. J. 459 (2023) 141502.
[6] C. Lin, X. Li, T. Wu, et al., BMEMat 1 (2023) e12007.
[7] X. Liu, Z. Ye, Q. Xiang, et al., Chem 9 (2023) 1464–1476.
[8] K. Chang, Y. Zhao, M. Wang, et al., Chem. Eng. J. 459 (2023) 141539.
[9] C. Li, Y. Zhang, Z. Ye, S.E.J. Bell, Y. Xu, Nat. Protoc. 18 (2023) 2717–2744.
[10] H.J. Han, S.H. Cho, S. Han, et al., Adv. Mater. 33 (2021) 2105199.
[11] F. Li, X. Mu, X. Tang, et al., Angew. Chem. Int. Ed. 62 (2023) e202218055.
[12] X. Wang, W. Shi, S. Wang, et al., J. Am. Chem. Soc. 141 (2019) 5856–5862.
[13] L. Yang, Y. Peng, Y. Yang, et al., Adv. Sci. 6 (2019) 1900310.
[14] P. Miao, J. Wu, Y. Du, Y. Sun, P. Xu, J. Mater. Chem. C 6 (2018) 10855–10860.
[15] M.G. Kim, M. Jue, K.H. Lee, et al., ACS Nano 17 (2023) 18332–18345.
[16] Q. Lv, J. Tan, Z. Wang, et al., Nat. Commun. 14 (2023) 2717.
[17] X. Wang, L. Guo, Angew. Chem. Int. Ed. 59 (2020) 4231–4239.
[18] L. Qiao, Y. Shen, S. Zhang, et al., BMEMat 1 (2023) e12011.
[19] Y. Ru, Y. Chen, X. Yu, et al., Chem. Eng. J. 475 (2023) 146158.
[20] Z. Hu, X. Liu, P.L. Hernández-Martínez, et al., InfoMat 4 (2022) e12290.
[21] J. Seo, Y. Kim, J. Lee, et al., J. Mater. Chem. A 10 (2022) 13298–13304.
[22] X. Fan, D. Zhao, Z. Deng, et al., Small 19 (2023) 2208036.
[23] X. Fan, X. He, X. Ji, et al., Inorg. Chem. Front. 10 (2023) 1431–1435.
[24] L. Ouyang, X. Fan, Z. Li, et al., Chem. Commun. 59 (2023) 1625–1628.
[25] Y. Zhao, T. Huang, X. Zhang, et al., BMEMat 1 (2023) e12006.
[26] N. Singh, J. Prakash, M. Misra, A. Sharma, R.K. Gupta, ACS Appl. Mater. Interfaces 9 (2017) 28495–28507.
[27] Z. Li, L. Luo, M. Li, et al., Nat. Commun. 12 (2021) 6698.
[28] H. Wang, F. Zhang, M. Jin, et al., Mater. Today Phys. 30 (2023) 100944.
[29] X. He, L. Hu, L. Xie, et al., J. Colloid Interf. Sci. 634 (2023) 86–92.
[30] X. He, Z. Li, J. Yao, et al., iScience 26 (2023) 107100.
[31] Y. Chen, Y. Wang, J. Yu, et al., Adv. Sci. 9 (2022) 2105869.
[32] X. Liu, C. Xing, F. Yang, et al., Adv. Energy Mater. 12 (2022) 2201009.
[33] X. Liu, L. Yang, M. Huang, et al., Appl. Catal. B: Environ. 319 (2022) 121887.
[34] T. Dong, X. Liu, Z. Tang, et al., Appl. Catal. B: Environ. 326 (2023) 122176.
[35] W. Wang, G. Zhang, Q. Wang, et al., Chin. Chem. Lett. 35 (2024) 109193.
[36] Q. Han, C. Wu, H. Jiao, et al., Adv. Mater. 33 (2021) 2008180.
[37] R. Jia, Y. Wang, C. Wang, et al., ACS Catal. 10 (2020) 3533–3540.
[38] T. Wang, J. Zhou, W. Wang, Y. Zhu, J. Niu, Chin. Chem. Lett. 33 (2022) 2121–2124.
[39] X. Zhang, L. Luo, R. Yun, et al., ACS Sustain. Chem. Eng. 7 (2019) 13856–13864.
[40] W. Chen, W. Mao, Z. Liu, et al., J. Hazard. Mater. 459 (2023) 132188.
[41] Y. Wang, Y. Zhang, X. zhu, Y. Liu, Z. Wu, Appl. Catal. B: Environ. 316 (2022) 121610.
[42] F. Zuo, L. Wang, T. Wu, et al., J. Am. Chem. Soc. 132 (2010) 11856–11857.
[43] G. Liu, W. Jaegermann, J. He, V. Sundström, L. Sun, J. Phys. Chem. B 106 (2002) 5814–5819.
[44] X. Chen, L. Liu, P.Y. Yu, S.S. Mao, Science 331 (2011) 746–750.
[45] L. Yao, L. Ouyang, J. Lv, P. Dai, L. Zhu, Microchem. J. 166 (2021) 106221.
[46] H. Zhang, L. Sun, Y. Zhang, et al., Chin. Chem. Lett. 29 (2018) 981–984.
[47] H. Zhang, N. Zhao, H. Li, et al., ACS Appl. Mater. Interfaces 14 (2022) 51253–51264.
[48] R.R. Jones, C. Miksch, H. Kwon, et al., Adv. Mater. 35 (2023) 2209282.
[49] Z. Liu, L. Wang, W. Bian, M. Zhang, J. Zhan, RSC Adv. 7 (2017) 3117–3124.
[50] X.X. Han, R.S. Rodriguez, C.L. Haynes, Y. Ozaki, B. Zhao, Nat. Rev. Method. Prime. 1 (2022) 87.
[51] L. Zhou, J. Zhou, W. Lai, et al., Nat. Commun. 11 (2020) 1785.